Faculty Publications -- Chemistry Department   Published Research - Department of Chemistry

2019

Machine Learning Enabled Prediction of Mechanical Properties of Tungsten Disulfide Monolayer

Xinyu Wang
Shandong University, xyw@sdu.edu.cn

Dan Han
Shandong University

Yang Hong
University of Nebraska - Lincoln

Haiyi Sun
Shandong University

Jingzhi Zhang
Shandong University

See next page for additional authors

Follow this and additional works at: https://digitalcommons.unl.edu/chemfacpub

Part of the Analytical Chemistry Commons, Medicinal-Pharmaceutical Chemistry Commons, and the Other Chemistry Commons

Authors

Xinyu Wang, Dan Han, Yang Hong, Haiyi Sun, Jingzhi Zhang, and Jingchao Zhang

Machine Learning Enabled Prediction of Mechanical Properties of Tungsten Disulfide Monolayer

Xinyu Wang,*,[†] Dan Han,[†] Yang Hong,[§] Haiyi Sun,[†] Jingzhi Zhang,[‡] and Jingchao Zhang*,[∥]

[†]Institute of Thermal Science and Technology and [‡]School of Energy and Power Engineering, Shandong University, Jinan 250061, China

[§]Department of Chemistry and [∥]Holland Computing Center, University of Nebraska-Lincoln, Lincoln, Nebraska 68588, United States

ABSTRACT: One of two-dimensional transition metal dichalcogenide materials, tungsten disulfide (WS_2), has aroused much research interest, and its mechanical properties play an important role in a practical application. Here the mechanical properties of h-WS_2 and t-WS_2 monolayers in the armchair and zigzag directions are evaluated by utilizing the molecular dynamics (MD) simulations and machine learning (ML) technique. We mainly focus on the effects of chirality, system size, temperature, strain rate, and random vacancy defect on mechanical properties, including fracture strain, fracture strength, and Young's modulus. We find that the mechanical properties of h-WS_2 surpass those of t-WS_2 due to the different coordination spheres of the transition metal atoms. It can also be observed that the fracture strain, fracture strength, and Young's modulus decrease when temperature and vacancy defect ratio are enhanced. The random forest (RF) supervised ML algorithm is employed to model the correlations between different impact factors and target outputs. A total number of 3600 MD simulations are performed to generate the training and testing dataset for the ML model. The mechanical properties of WS_2 (i.e., target outputs) can be predicted using the trained model with the knowledge of different input features, such as WS_2 type, chirality, temperature, strain rate, and defect ratio. The mean square errors of ML predictions for the mechanical properties are orders of magnitude smaller than the actual values of each property, indicating good training results of the RF model.
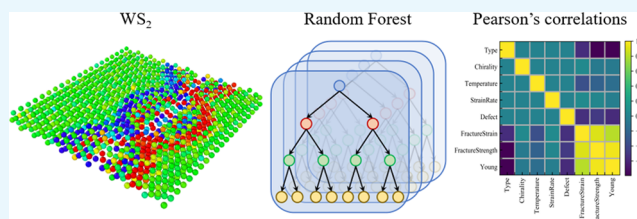
1. INTRODUCTION

Two-dimensional (2D) materials have attracted the research interest from both academia and industries due to their glorious properties,[1−4] since graphene was successfully obtained from the graphite for the first time using mechanical exfoliation in 2004.[5] Although graphene possesses outstanding thermal, electrical, and mechanical properties,[6−8] the characteristic of zero band gap limits its direct applications in nanoelectronics, such as field effect transistors (FETs),[9] which drives the researcher to discover novel 2D materials with the desired semiconducting features. Transition metal dichalcogenides (TMDCs) are emerging materials with fascinating physical properties,[10,11] which have the chemical formula of MX_2 (M is a transition metal atom and X is a chalcogen atom). TMDCs have direct band gaps and can be widely used in FETs,[12] planar batteries,[13] and nanogenerators.[14] In the TMDC family, it has been demonstrated that tungsten disulfide (WS_2) has a direct energy gap of ~2 eV, a strong spin−orbit coupling, and the splitting of valence bands at K/K′ points, which ensures that WS_2 be the next-generation candidate in nanoelectronics, spintronics, and optoelectronics.[15−17] Ovchinnikov et al. have reported that the WS_2-based FETs displayed excellent electrical properties,[18] such as the n-type behavior with a high room-temperature on/off current ratio of ~10^6. Moreover, at low temperatures, the metallic behavior in the WS_2-based FETs was possessed at high

charge carrier densities and mobilities as high as ~140 cm^2 V^{-1} s^{-1} (above 300 cm^2 V^{-1} s^{-1} for bilayers). The thermal conductivity of WS_2 monolayer has been evaluated by experimental measurement[19] and first-principles theory,[20] which were equal to 32 W $m^{-1}K^{-1}$ and 31.8 W m^{-1} K^{-1}, respectively.

Although the electrical and thermal properties of WS_2 have been widely investigated, its mechanical properties such as the deformation and fracture under different temperatures and pressures have not been given enough attention. Several works have been performed to evaluate the mechanical properties of several other TMDCs. Bertolazzi et al. experimentally measured Young's moduli of monolayer and bilayer MoS_2 and the values were 270 ± 100 GPa and 200 ± 100 GPa, respectively.[21] By making use of the first-principles theory, Young's moduli of MoS_2 were investigated to be 200.2 ± 0.2 GPa and 200.4 ± 0.4 GPa in armchair and zigzag directions, respectively; the corresponding ultimate strengths were equal to 23.6 GPa and 16.1 GPa.[22] The averaged Young's modulus of suspended MoS_2 nanosheets was measured to be 330 ± 70 GPa, which was equivalent to graphene oxide.[23] It has been displayed that the mechanical properties of WSe_2 were

independent of the layer thickness.[24] For multilayer WSe_2, the fracture strength and fracture strain were 12.4 GPa and 0.073, respectively, and Young's modulus was 167.3 ± 6.7 GPa. Also, by utilizing the molecular dynamics (MD) simulation, $MoSe_2$ monolayer was found to possess different fracture strengths and fracture strains along the armchair and zigzag directions, which both decreased with increased temperature.[25] However, to the best of our knowledge, there are no systematical investigations about the mechanical properties of WS_2 under the effects of different phases, chiralities, temperatures, strain rates, and vacancy defects. Therefore, it is worth evaluating the mechanical responses of WS_2 to enrich this research gap.

Applications of machine learning (ML) techniques in material science have attracted growing attention in recent years.[26−28] Most of the models used in property predictions are supervised ML algorithms, meaning the model needs to be trained on large amounts of dataset to find the inherent correlations between the input features and output targets. The dataset for ML algorithms can be obtained either experimentally or numerically. For numerical studies, the generation of the training dataset is computationally intensive and time consuming, which creates a tremendous challenge. Recently, with the help of high-performance supercomputers, the training dataset can be obtained within a reasonable amount of time by carefully selecting and designing the sampling properties and data structures. Random forest (RF) is a versatile and robust ensemble ML algorithm based on decision trees for both classification and regression problems,[29] which can gain accuracy as the trees grow without suffering from overtraining. It has been successfully employed in several fields such as image classification,[30] voice recognition,[31] weather forecast,[32] and material classification.[33] On account of its extraordinary capability, the RF algorithm is utilized to predict the mechanical properties of WS_2 with the help of MD generated training dataset in this work.

TMDCs possess several structural phases on account of the different coordination spheres of the transition metal atoms. The features of two stable phases are trigonal prismatic (h-phase) and octahedral (t-phase) coordination of metal atoms. In this work, we systematically apply MD and ML techniques to investigate the effects of WS_2 type, chirality, size, temperature, strain rate, and defect ratio on mechanical properties. First, the chirality dependence and size dependence of mechanical properties of WS_2 are evaluated. Afterward, we analyze the effects of temperature, strain rate, and vacancy defect on fracture performances of WS_2. Finally, after training the ML algorithm with MD results, ML is further applied to predict the fracture strains, fracture strengths, and Young's moduli on h-WS_2 and t-WS_2.

2. METHODOLOGY

Random forest machine learning algorithm is an ensemble technique that can be used in both classification and regression tasks. The RF algorithm is composed of multiple decision trees (DTs)[34] and a technique called Bootstrap Aggregation, also known as bagging.[35] It utilizes the same learning algorithm but train each learner on a different set of data. The RF algorithm combines multiple DTs in determining the final output rather than relying on individual DTs. Mean square errors (MSEs) are applied to assess the model performances, which is calculated by the following equation

$$\mathrm{MSE}(y, \hat{y}) = \frac{1}{n} \sum_{i=0}^{n-1} (y_i - \hat{y}_i)^2 \tag{1}$$

where n is the number of samples, i is the sample index, y is the target value, and $\hat{y}$ is the predicted value. An illustration of the RF algorithm is shown in Figure 1. Each box with a blue
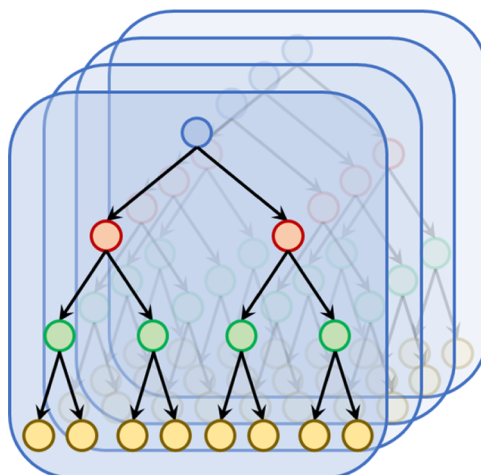

Figure 1. Illustration of random forest machine learning algorithm.

background color represents an individual DT, and the RF is composed of an ensemble of DTs. There are two general issues with ML model trainings, i.e., overfitting and underfitting. The overfitting problem can be caused by the ML algorithm being too complex for the training data or the dataset is too small. An overfitted model will predict the training data with very high accuracy or very low MSE but has poor generalization performances on the test or new data. This is due to the fact that the model is learning from the noise of the data instead of the actual relationships between variables. In contrast to overfitting, an underfitted model could not describe the training data and therefore misses the trends, which also means the model cannot be generalized to new data. For example, underfitting could occur when using a linear model to describe a second-order polynomial dataset. Since the RF algorithm is a very versatile approach, underfitting is unlikely to occur for the dataset used in this work. To battle the overfitting problem and validate the trained model, a 10-fold cross-validation is used.

All simulations are performed utilizing the open source software Large-scale Atomic/Molecular Massively Parallel Simulator (LAMMPS).[36] Figure 2 displays the atomic configurations of h-WS_2 and t-WS_2. The pink solid spheres represent W atoms, and yellow solid spheres represent S
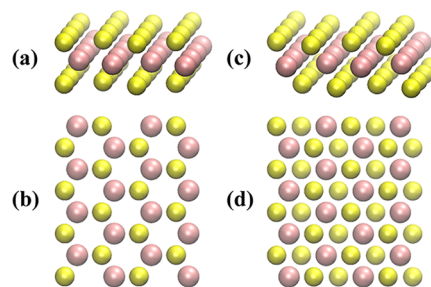

Figure 2. (a, b) Side and top views of h-WS_2. (c, d) Side and top views of t-WS_2.

atoms. The armchair and zigzag chiralities are along the x direction and y direction, respectively. To model the W and S atom interactions within the h-WS$_2$ and t-WS$_2$ monolayers, the two different Stillinger−Weber potentials developed by Jiang et al. are employed, respectively.[37] The time step is set as 0.5 fs. Periodic boundary conditions are employed in all directions to eliminate the edge effects. Moreover, we add a vacuum layer of 10 nm in the z direction to avoid the atomic interaction with the system image. The simulation process is as follows: we first relax the original WS$_2$ structure using the Polak−Ribiere version of the conjugate gradient algorithm. The system is then switched to the isothermal−isobaric ensemble (NPT) to further eliminate the system residuary stress at 0 bar for 300 ps. Thereafter, the WS$_2$ system is elongated with a designated strain rate, where the elongation of WS$_2$ system will abide by the following equation

$$L_t = L_0(1 + \varepsilon \mathrm{d}t) \qquad (2)$$

where L_0 is the original system length, L_t is the length of the system at time t, and ε is the strain rate. We apply the uniaxial displacement along either the armchair or zigzag direction and hold the pressure along the other two directions as zero. For each simulation, five independent simulations with different velocity seeds (initial conditions) are performed, and the final values are calculated by averaging each simulation with the standard deviations shown as error bars.

We perform 3600 (2 types × 2 directions × 6 temperatures × 5 strain rates × 6 defect ratios × 5 initial conditions) MD simulations as input files to generate enough data points for the ML algorithms, which are organized in a hierarchical structure. When 3600 MD simulations are finished, we collect all strain−stress results and postprocess them using a MATLAB script. Afterward, the fracture strain, fracture strength, and Young's modulus with a given type, direction, temperature, strain rate, and vacancy can be extracted. Finally, 80% of MD results are then inputted into the ML algorithms for the model training and 20% of the data points are isolated to test the ML model performance.

3. RESULTS AND DISCUSSION

3.1. Effects of Chirality and Size.
First, the chirality dependence of the mechanical properties of WS$_2$ is studied. The system is stretched after the relaxation process in NPT at 1 K by employing a constant strain rate of 1×10^{-4} ps^{-1} in the armchair or zigzag direction. The strain−stress relations for h-WS$_2$ and t-WS$_2$ with size 5.42 × 6.26 nm^2 ($x \times y$ nm^2) are depicted in Figure 3. At the small strain level, the linear variation in the strain−stress curves can be observed from Figure 3, which reveals the elastic mechanical response. On the contrary, the relation between stress and the applied strain under high strain values becomes nonlinear, and plastic deformation generates for both h-WS$_2$ and t-WS$_2$. Moreover, with the further increased strain, the stress finally arrives at the maximum value and suddenly drops down, which is due to the system fracture. We attribute this elastic−plastic deformation transition to the phase transformation in WS$_2$ during elongation.[25]

The fracture strength is defined as the maximum stress the system can withstand, and the corresponding strain represents the fracture strain. The h-WS$_2$ possesses the higher averaged fracture strength and fracture strain in the armchair and zigzag directions, which are equal to 14.74 GPa, 0.22 and 14.09 GPa, 0.25, severally. However, the lower fracture strengths and
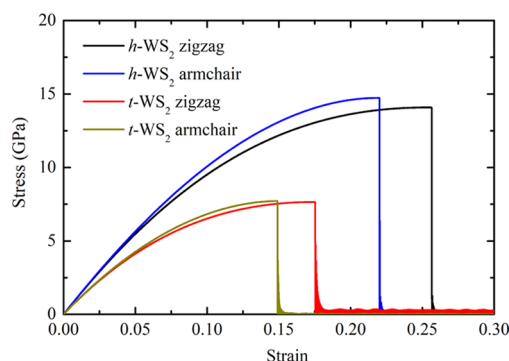

Figure 3. Strain−stress profiles of h-WS$_2$ and t-WS$_2$ in the zigzag and armchair directions at 1 K and a strain rate of 1×10^{-4} ps^{-1}.

strains for t-WS$_2$ are 7.72 GPa, 0.15 and 7.65 GPa, 0.17, respectively. Afterward, Young's moduli of WS$_2$ are calculated by fitting the low strain level (<0.02) stress−strain curves. For h-WS$_2$, the calculated Young's moduli are 119.44 GPa and 117.89 GPa along the armchair and zigzag directions, respectively, and for t-WS$_2$, the corresponding Young's moduli are 95.38 GPa and 94.11 GPa. We attribute the mechanical discrepancy between h-WS$_2$ and t-WS$_2$ to the phase structure difference. Due to the different coordination spheres of the transition metal atoms, WS$_2$ displays the discrepant bond stretching and bending interactions in these two phases, which subsequently leads to diverse physical properties. For instance, h-WS$_2$ acts as a semiconductor, whereas t-WS$_2$ similar to metal has no band gap.[38] From Figure 3, we also find that there are weak anisotropies in both h-WS$_2$ and t-WS$_2$ owing to the variations of bond length (W−S and S−S) and bond angle (S−W−S) under the tensile stress.[39] To exhibit the fracture differences between h-WS$_2$ and t-WS$_2$, Figure 4 displays the crack propagations along the armchair direction. It can be observed that the force required to break the bonding in t-WS$_2$ is much lower than that in h-WS$_2$. This phenomenon coincides with the results displayed in Figure 3. The similar phenomenon has been reported in other 2D materials.[22,40,41] It has been reported that the calculated Young's moduli of borophene along the armchair and zigzag directions at 1 K are ∼1203 GPa and ∼562 GPa, respectively, and the obvious difference mechanical properties between disparate chirality could be observed.[40] Similarly, Mortazavi demonstrated that the ultimate tensile strength of C$_3$N monolayer in the armchair direction was around 2.4 GPa larger than that in the zigzag direction.[41] It should be noted that even though the mechanical properties along different directions are similar at a low strain level, the deformation behaviors at a high strain level depict the significant discrepancy, which consists well with the first-principles calculation of MoS$_2$ monolayer.[22]

In general, the physical properties of 2D materials exhibit size dependence with the effect of the material edge. For example, due to phonon boundary scattering, the thermal conductivities of MoS$_2$ and MoSe$_2$ will decrease with the reduction of the material length.[11] Hence, it is significant to investigate the size dependence of the mechanical properties of WS$_2$. Here we build other three dimensions of h-WS$_2$ and t-WS$_2$ monolayers with sizes 1.08 × 1.25, 10.84 × 12.52, and 21.69 × 25.04 nm^2, aside from the previous 5.42 × 6.26 nm^2. The relations between calculated fracture strain, fracture strength, and Young's moduli and system sizes are depicted in Figure 5. We can notice that the fracture strains, fracture
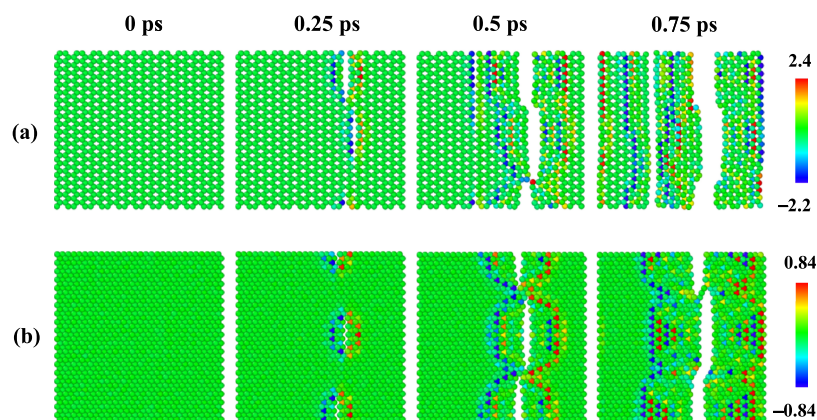
Figure 4. Crack formation and propagation in the armchair direction of (a) h-WS$_2$ and (b) t-WS$_2$. The color bar denotes the atomic forces in the unit of eV Å^{-1}.
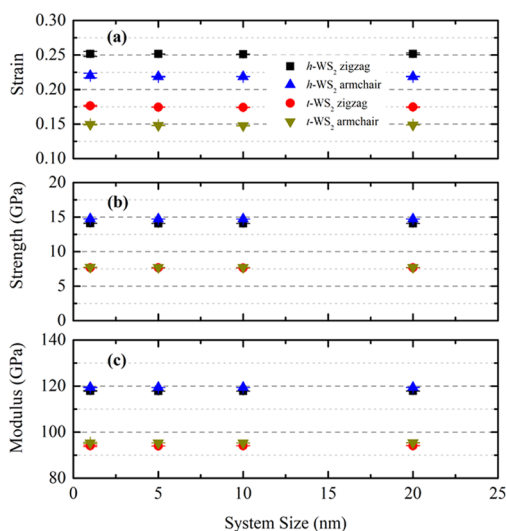

Figure 5. Convergence of (a) fracture strain, (b) fracture strength, and (c) Young's modulus with system dimensions at 1 K and a strain rate of 1×10^{-4} ps^{-1}. Each data point is averaged from five independent simulations with different initial conditions. The error bars represent standard deviations.

Figure 6. Variations of strain−stress curves with temperature from 1 to 500 K for h-WS$_2$ in the (a) zigzag and (b) armchair directions with a constant strain rate of 1×10^{-4} ps^{-1}.

strengths, and Young's moduli of h-WS$_2$ and t-WS$_2$ keep convergent with the varied size, which manifests that WS$_2$ shows size-independent in current size range. Therefore, we choose the system of 5.42 × 6.26 nm^2 in subsequent MD simulations to save computational cost.

3.2. Effects of Temperature and Strain Rate. In practical applications, the nanoelectronics is frequently operated under versatile physical environment, for example, extreme temperature and high loading strain rate, which can alter the mechanical properties of structural materials or even cause unexpected structural failures. Therefore, here we analyze the influences of temperature and strain rate on the mechanical properties of the WS$_2$.

Different temperatures of 1, 100, 200, 300, 400, and 500 K are employed in the NPT ensemble. In view of the similar variation trends for t-WS$_2$, the strain−stress profiles for h-WS$_2$ variations with temperature are only displayed in Figure 6. It can be found that the increased temperature makes the fracture phenomena arise earlier in both directions for h-WS$_2$. The fracture strain, fracture strength, and Young's modulus with different temperatures are also calculated by using the same
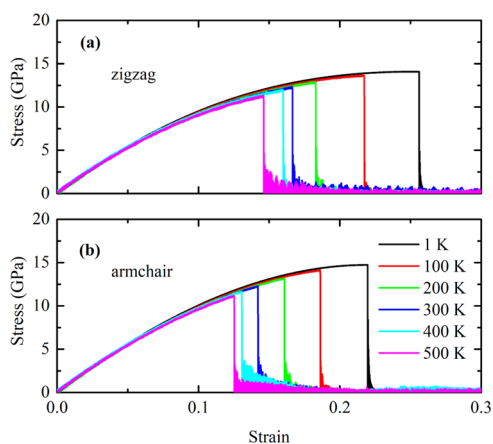
method in the above studies, which are depicted in Figure 7. When the temperature increases from 1 to 500 K, the fracture strains along the armchair and zigzag directions decline monotonically from 0.22 to 0.13, from 0.25 to 0.14 (for h-WS$_2$) and from 0.15 to 0.06, from 0.17 to 0.07 (for t-WS$_2$); the corresponding fracture strengths accordingly decrease by 22.79%, 19.92% and 40.65%, 39.82%. This temperature-induced reduction in the WS$_2$ mechanical properties resembles with other 2D materials.[42,43] The effect of temperature may stem from the following three reasons: (1) The kinetic energy is transferred into strain energy during the deformation due to tensile stress, and the kinetic energy of atoms increases at the elevated temperature, which decreases the strain energy.[44] (2) Due to the applied tensile stress, the binding energy between atoms decreases, which generates the lower energy barrier for breaking the chemical bonds.[25,44,45] (3) The thermal fluctuations of atoms enhance at elevated temperature, and cause that the lower energy barrier is more likely to be overcome.[42] Based on the above discussion, we can deduce that high temperature accelerates the fracture formation and propagations in both h-WS$_2$ and t-WS$_2$. Although the fracture strain and fracture strength exhibit the obvious temperature dependence, the temperature sensitivity of Young's modulus is relatively slight. The calculated Young's moduli along the armchair and zigzag directions are slightly reduced from 119.44 to 113.59 GPa, from 117.89 to 111.77 GPa (for h-WS$_2$), and
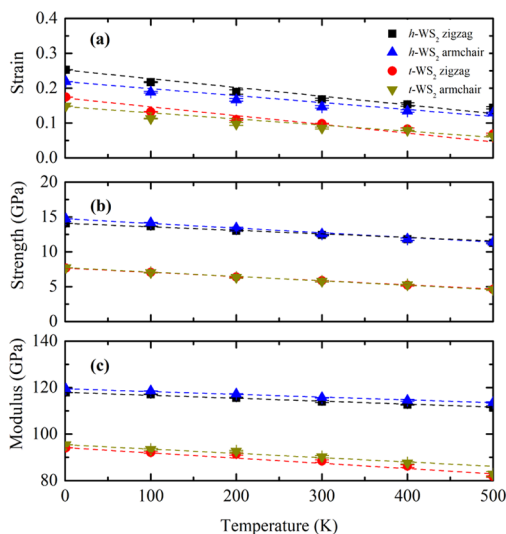
Figure 7. Effects of temperature on (a) fracture strain, (b) fracture strength, and (c) Young's modulus of h-WS$_2$ and t-WS$_2$ in the zigzag and armchair directions with a constant strain rate of 1×10^{-4} ps^{-1}. Each data point is averaged from five independent simulations with different initial conditions. The error bars represent standard deviations.

from 95.38 to 82.81 GPa, from 94.11 to 81.75 GPa (for t-WS$_2$), severally. It can also be observed that since t-WS$_2$ are apt to deform, the temperature sensitivities of the mechanical properties of t-WS$_2$ are more obvious than those of h-WS$_2$.

Moreover, we set different strain rates of 1×10^{-4} (i.e., the aforementioned strain rate), 2.5×10^{-4}, 5×10^{-4}, 1×10^{-3}, and 2.5×10^{-3} ps^{-1} in MD simulations to study the effect of strain rate. The relations between strain rate and fracture strains, fracture strengths, and Young's moduli of h-WS$_2$ and t-WS$_2$ at 1 K are shown in Figure 8. We observe that the fracture strains and fracture strengths keep almost unchanged and the calculated Young's moduli have an unconspicuous reduction with an increased strain rate. Our results agree well with the previous results about the effect of strain rate on the mechanical properties of MoSe$_2$.[25]
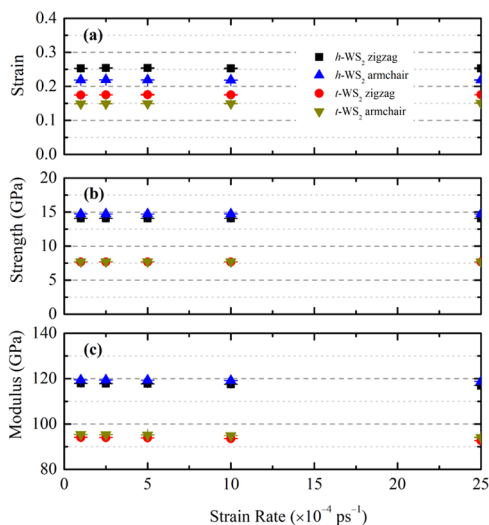

Figure 8. Effect of strain rate from 1 to 25×10^{-4} ps^{-1} on (a) fracture strain, (b) fracture strength, and (c) Young's modulus of h-WS$_2$ and t-WS$_2$ in the zigzag and armchair directions at 1 K.

3.3. Effect of Vacancy Defect.

Previous investigations have reported that vacancy defects can alter and tune the physical and chemical properties of 2D materials.[46,47] It has been observed that the electronic transport was transformed by generating defect-induced localized states in defective MoS$_2$.[46] Furthermore, the increasing vacancy defects decreased the thermal conductivity of graphene due to the enhanced phonon defect scattering and the suppressed low frequency phonons.[47] The general method for the synthesis of high-quality WS$_2$ is chemical vapor deposition on SiO$_2$/Si,[48] hexagonal boron nitride,[49] or reusable Au foil substrates.[50] However, owing to the imperfection of chemically grown process in 2D materials, structure defects including vacancies are particularly noticeable.[51] Therefore, it is worthy of evaluating mechanical responses with different vacancy defect ratios. In graphene monolayer, the type of defect can also affect the thermal and mechanical properties, which includes the single-vacancy defect, double-vacancy defect, multi-vacancy defect, and Stone−Wales defect.[52−55] To investigate the effect of defects on the mechanical properties in WS$_2$, we created random defects including different vacancy defect types with vacancy concentration from 0 to 5% in both h-WS$_2$ and t-WS$_2$.

Effects of vacancy defect on the mechanical properties of h-WS$_2$ and t-WS$_2$ at 1 K and 1×10^{-4} ps^{-1} are shown in Figure 9.
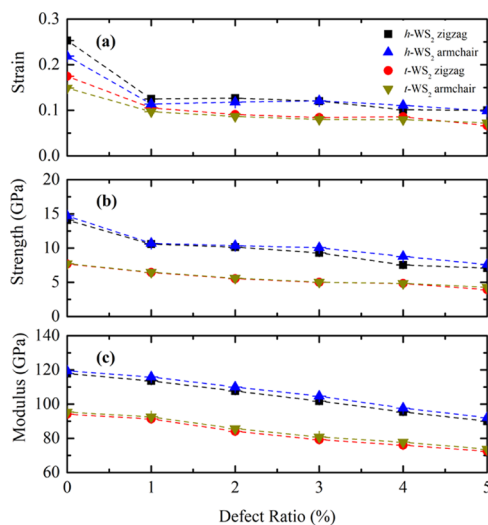

Figure 9. Effects of defect from 0 to 5% on (a) fracture strain, (b) fracture strength, and (c) Young's modulus of h-WS$_2$ and t-WS$_2$ in the zigzag and armchair directions at 1 K and a strain rate of 1×10^{-4} ps^{-1}.

When the vacancy defect ratio increases from 0 to 5%, the fracture strengths for h-WS$_2$ and t-WS$_2$ in the armchair and zigzag directions will decrease by 48.35%, 49.67% and 44.26%, 48.73%, respectively; the decline proportions of the fracture strain are 54.89%, 60.41% and 51.30%, 62.10%. Moreover, the corresponding Young's moduli strictly reduce from 119.44 to 92.15 GPa, from 117.89 to 90.00 GPa and from 95.38 to 73.62 GPa, from 94.11 to 72.44 GPa with vacancy defects up to 5%. The similar effect of vacancy defects has been observed in other 2D systems.[22,42,56] Gan et al. using the first-principles theory investigated the effect of regular vacancy defect, i.e., 3 × 3 × 1 MoS$_2$ supercell structure with one sulfur missing vacancy, on Young's moduli and ultimate strengths. They found that this vacancy defect could reduce Young's moduli and fracture strengths from 200.0 ± 0.2 to 194.2 ± 0.2 GPa,

from 23.6 to 17.8 GPa and from 200.4 $\pm$ 0.2 to 191.8 $\pm$ 0.4 GPa, from 16.1 to 15.4 GPa in the armchair and zigzag directions, respectively.[22] The defect dependence of mechanical properties of phosphorene was investigated by utilizing the MD simulations. When the vacancy concentration was 2%, in comparison with the pristine structure, the fracture strength of phosphorene along the armchair and zigzag directions decreased by 39% and 41%, respectively; the corresponding fracture strains dropped by 34% and 39%.[42] The effect of vacancy defect may be attributed to the following points: (1) The WS$_2$ monolayers have stress concentration at the vacancy defects, where the stress concentration can affect the fracture behaviors.[57,58] (2) The fracture of WS$_2$ monolayers is originated by the nucleation of a vacancy defect, and the increasing vacancy defect enhances the nucleation phenomenon. (3) The integrity of pristine WS$_2$ can be broken by vacancy defects, and the vacancies disorder and weaken the W−S bond interaction.[22,42,56] As a consequence, the subsistent vacancy defects accelerate the formation and extension of crack under the tensile stress.

3.4. Machine Learning Predictions. The mechanical properties of h-WS$_2$ and t-WS$_2$ are calculated in both zigzag and armchair directions under six different temperatures, five different strain rates, and six different defect ratios. Therefore, each data point is associated with five input features, i.e., type, chirality, temperature, strain rate, and defect ratio, and three output target values, i.e., fracture strain, fracture strength, and Young's modulus. The dataset is split into training and testing with portions of 80% and 20%, respectively. We use a 10-fold cross-validation to inspect the accuracies of trained models for the sake of flagging overfitting or selection bias. It should be noticed that the dataset is split using a stratified method rather than the random method, which can ensure the effect of the most important feature on the training results. Figure 10
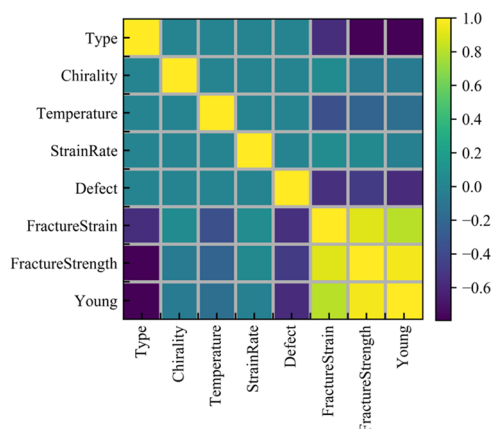

Figure 10. Pearson's correlations among different features and target outputs.

displays the evaluated Pearson's correlation between each pair of input features and output targets. The correlation coefficient ranges from −1 to 1 corresponding to the strongest negative and positive correlations. It is observed that the type of WS$_2$ has the strongest impact on its fracture strain, fracture strength, and Young's modulus. However, since there are only two categories for the WS$_2$ types, it is less likely to have a biased data selection compared to other features. Therefore, the second most significant impact factor, i.e., defect, is used for the data split. We employ the feature scaling to get better

results and normalize all input values between 0 and 1 to uniform the distribution of feature spaces.

To find the best parameter for the RF algorithm, a grid search method is used to determine the optimal values to be used for the hyperparameters. Two hyperparameters, i.e., maxdepth and n-estimator, are optimized in the grid search. The max-depth refers to the maximum depth of the tree and n-estimator is the number of the trees in the forest. Ideally, the performance of the model will increase with the growing number of trees but one needs to be cautious to avoid the overfitting problems. A list of max-depth values ranging from 3 to 10 is explored. For n-estimator, different values of 1, 10, 100, 1000, and 2000 are used. The best combinations of maxdepth and n-estimator are 9 and 1000, respectively. A 10-fold cross-validation is conducted to verify the accuracy of the trained model as well as overfitting. Once the model is trained, the RF regressor is used to predict the mechanical properties of WS$_2$ on the test data. As shown in Figure 11, the predicted
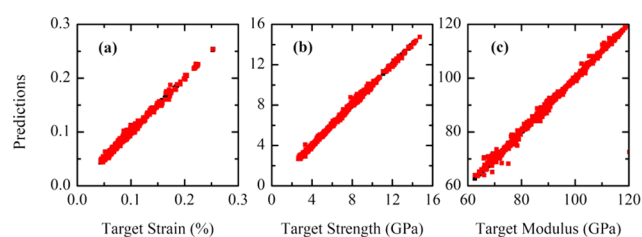

Figure 11. Comparisons of ML predicted (a) fracture strain, (b) fracture strength, and (c) Young's modulus with MD simulation results. The red and black square dots represent ML predicted and target values, respectively.

mechanical properties from the trained RF model soundly match those generated from the MD simulations, indicating the validity of the ML model. The overall MSEs for fracture strain, fracture strength, and Young's modulus are 9.2×10^{-6}, 1.9×10^{-2} GPa, and 3.8 GPa, respectively, which are several orders of magnitude lower than the corresponding properties.

Even though the mechanical properties of h-WS$_2$ and t-WS$_2$ monolayers can be successfully predicted by the RF regressor, it is worth noting that there are some limitations associated with the current trained model. To save computational time, only five impact factors including system type, chirality, temperature, strain rate, and defect were considered in this work. Therefore, the model cannot be employed on systems where other impact factors such as isotopic doping or chemical functionalization existence; otherwise, the addition of each new impact factor would drastically bring out the increase of computational time. Meanwhile, the model is specifically trained on the mechanical properties of WS$_2$, and new train datasets are required for other materials. Nevertheless, the successful implementation of the machine learning technique to mechanical property prediction sheds some light on datadriven materials studies and paves the way for solving engineering problems using the state-of-the-art artificial intelligence approach.

4. CONCLUSIONS

In conclusion, the mechanical properties of h-WS$_2$ and t-WS$_2$ monolayers are investigated systematically using the MD simulations and machine learning technique. The trained ML model can predict the mechanical properties of WS$_2$ with the knowledge of input features including WS$_2$ type, chirality,

temperature, strain rate, and defect ratio. The MSEs between ML predicted and MD simulation generated results are 9.2×10^{-6}, 1.9×10^{-2} GPa, and 3.8 GPa for fracture strain, fracture strength, and Young's modulus, respectively, which are several orders of magnitude lower than the corresponding properties. On account of the different coordination spheres of the transition metal atoms, the fracture strain, fracture strength, and Young's modulus of t-WS$_2$ are lower than those of h-WS$_2$. The fracture strain reduction ratios of h-WS$_2$ and t-WS$_2$ in the armchair and zigzag directions are 41.20%, 43.08% and 57.78%, 60.82%, respectively, as the temperature enhances from 1 to 500 K. Furthermore, the fracture strengths accordingly decrease by 22.79%, 19.92% and 40.65%, 39.82%. We attribute the decrease of mechanical properties to the decreased strain energy, the decreased binding energy, and the enhanced atoms thermal fluctuations. The fracture strains and fracture strengths are almost unchanged, and the calculated Young's moduli have the trivial reduction with the increased strain rate. The increasing vacancy defect from 0 to 5% is found to decrease the fracture strain, fracture strength, and Young's modulus on account of the stress concentrations, the increasing fracture nucleation, the disorderly W–S bonds, and the material softening.

■ AUTHOR INFORMATION

Corresponding Authors
*E-mail: xyw@sdu.edu.cn (X.W.).
*E-mail: zhang@unl.edu (J.Z.).

ORCID
Xinyu Wang: 0000-0003-4143-334X
Jingchao Zhang: 0000-0001-5289-6062

Notes
The authors declare no competing financial interest.

■ REFERENCES

(1) Xiong, Z.; Wang, X.; Lee, K. H. K.; Zhan, X.; Chen, Y.; Tang, J. Thermal transport in supported graphene nanomesh. *ACS Appl. Mater. Interfaces* **2018**, *10*, 9211–9215.

(2) Wang, X.; Hong, Y.; Ma, D.; Zhang, J. Molecular dynamics study of thermal transport in a nitrogenated holey graphene bilayer. *J. Mater. Chem. C* **2017**, *5*, 5119–5127.

(3) Han, D.; Wang, X.; Ding, W.; Chen, Y.; Zhang, J.; Xin, G.; Cheng, L. Phonon thermal conduction in a graphene-C$_3$N heterobilayer using molecular dynamics simulations. *Nanotechnology* **2019**, *30*, No. 075403.

(4) Mortazavi, B.; Makaremi, M.; Shahrokhi, M.; Fan, Z.; Rabczuk, T. N-graphdiyne two-dimensional nanomaterials: semiconductors with low thermal conductivity and high stretchability. *Carbon* **2018**, *137*, 57–67.

(5) Novoselov, K. S.; Geim, A. K.; Morozov, S. V.; Jiang, D.; Zhang, Y.; Dubonos, S. V.; Grigorieva, I. V.; Firsov, A. A. Electric field effect in atomically thin carbon films. *Science* **2004**, *306*, 666.

(6) Bolotin, K. I.; Sikes, K. J.; Jiang, Z.; Klima, M.; Fudenberg, G.; Hone, J.; Kim, P.; Stormer, H. L. Ultrahigh electron mobility in suspended graphene. *Solid State Commun.* **2008**, *146*, 351–355.

(7) Balandin, A. A.; Ghosh, S.; Bao, W.; Calizo, I.; Teweldebrhan, D.; Miao, F.; Lau, C. N. Superior thermal conductivity of single-layer graphene. *Nano Lett.* **2008**, *8*, 902–907.

(8) Lee, C.; Wei, X.; Kysar, J. W.; Hone, J. Measurement of the elastic properties and intrinsic strength of monolayer graphene. *Science* **2008**, *321*, 385–388.

(9) Singh, A. K.; Yakobson, B. I. Electronics and magnetism of patterned graphene nanoroads. *Nano Lett.* **2009**, *9*, 1540–1543.

(10) Wang, Q. H.; Kalantar-Zadeh, K.; Kis, A.; Coleman, J. N.; Strano, M. S. Electronics and optoelectronics of two-dimensional transition metal dichalcogenides. *Nat. Nanotechnol.* **2012**, *7*, 699.

(11) Hong, Y.; Zhang, J.; Zeng, X. C. Thermal conductivity of monolayer MoSe$_2$ and MoS$_2$. *J. Phys. Chem. C* **2016**, *120*, 26067–26075.

(12) Radisavljevic, B.; Radenovic, A.; Brivio, J.; Giacometti, V.; Kis, A. Single-layer MoS2 transistors. *Nat. Nanotechnol.* **2011**, *6*, 147.

(13) Wan, J.; Bao, W.; Liu, Y.; Dai, J.; Shen, F.; Zhou, L.; Cai, X.; Urban, D.; Li, Y.; Jungjohann, K.; Fuhrer, M. S.; Hu, L. In situ investigations of Li-MoS$_2$ with planar batteries. *Adv. Energy. Mater.* **2014**, *5*, No. 1401742.

(14) He, M.; Lin, Y.-J.; Chiu, C.-M.; Yang, W.; Zhang, B.; Yun, D.; Xie, Y.; Lin, Z.-H. A flexible photo-thermoelectric nanogenerator based on MoS$_2$/PU photothermal layer for infrared light harvesting. *Nano Energy* **2018**, *49*, 588–595.

(15) Sik Hwang, W.; Remskar, M.; Yan, R.; Protasenko, V.; Tahy, K.; Doo Chae, S.; Zhao, P.; Konar, A.; Xing, H.; Seabaugh, A.; Jena, D. Transistors with chemically synthesized layered semiconductor WS$_2$ exhibiting 10^5 room temperature modulation and ambipolar behavior. *Appl. Phys. Lett.* **2012**, *101*, No. 013107.

(16) Zeng, H.; Liu, G.-B.; Dai, J.; Yan, Y.; Zhu, B.; He, R.; Xie, L.; Xu, S.; Chen, X.; Yao, W.; Cui, X. Optical signature of symmetry variations and spin-valley coupling in atomically thin tungsten dichalcogenides. *Sci. Rep.* **2013**, *3*, No. 1608.

(17) Perea-López, N.; Elías, A. L.; Berkdemir, A.; Castro-Beltran, A.; Gutiérrez, H. R.; Feng, S.; Lv, R.; Hayashi, T.; López-Urías, F.; Ghosh, S.; Muchharla, B.; Talapatra, S.; Terrones, H.; Terrones, M. Photosensor device based on few-layered WS$_2$ films. *Adv. Funct. Mater.* **2013**, *23*, 5511–5517.

(18) Ovchinnikov, D.; Allain, A.; Huang, Y.-S.; Dumcenco, D.; Kis, A. Electrical transport properties of single-layer WS$_2$. *ACS Nano* **2014**, *8*, 8174–8181.

(19) Peimyoo, N.; Shang, J.; Yang, W.; Wang, Y.; Cong, C.; Yu, T. Thermal conductivity determination of suspended mono- and bilayer WS$_2$ by Raman spectroscopy. *Nano Res.* **2015**, *8*, 1210–1221.

(20) Peng, B.; Zhang, H.; Shao, H.; Xu, Y.; Zhang, X.; Zhu, H. Thermal conductivity of monolayer MoS$_2$, MoSe$_2$, and WS$_2$: interplay of mass effect, interatomic bonding and anharmonicity. *RSC Adv.* **2016**, *6*, 5767–5773.

(21) Bertolazzi, S.; Brivio, J.; Kis, A. Stretching and breaking of ultrathin MoS$_2$. *ACS Nano* **2011**, *5*, 9703–9709.

(22) Gan, Y.; Zhao, H. Chirality effect of mechanical and electronic properties of monolayer MoS$_2$ with vacancies. *Phys. Lett. A* **2014**, *378*, 2910–2914.

(23) Castellanos-Gomez, A.; Poot, M.; Steele, G. A.; van der Zant, H. S. J.; Agraït, N.; Rubio-Bollinger, G. Elastic properties of freely suspended MoS$_2$ nanosheets. *Adv. Mater.* **2012**, *24*, 772–775.

(24) Zhang, R.; Koutsos, V.; Cheung, R. Elastic properties of suspended multilayer WSe$_2$. *Appl. Phys. Lett.* **2016**, *108*, No. 042104.

(25) Wang, X.; Hong, Y.; Wang, M.; Xin, G.; Yue, Y.; Zhang, J. Mechanical properties of molybdenum diselenide revealed by molecular dynamics simulation and support vector machine. *Phys. Chem. Chem. Phys.* **2019**, *21*, 9159–9167.

(26) Butler, K. T.; Davies, D. W.; Cartwright, H.; Isayev, O.; Walsh, A. Machine learning for molecular and materials science. *Nature* **2018**, *559*, 547–555.

(27) Ferguson, A.; Hachmann, J. Machine learning and data science in materials design: a themed collection. *Mol. Syst. Des. Eng.* **2018**, *3*, 429−430.

(28) Zhang, Y.; Ling, C. A strategy to apply machine learning to small datasets in materials science. *npj Comput. Mater.* **2018**, *4*, No. 25.

(29) Ho, T. K. In *Random decision forests*, Proceedings of the Third International Conference on Document Analysis and Recognition (Volume 1) - Volume 1, IEEE Computer Society, 1995; p 278.

(30) Zhu, L.; Wu, M. H.; Wan, X. K.; Zhao, N.; Xiong, W. Image recognition of rapeseed pests based on random forest classifier. *Int. J. Inf. Technol. Web Eng.* **2017**, *12*, 1−10.

(31) Zvarevashe, K.; Olugbara, O. O. In *Gender voice recognition using random forest recursive feature elimination with gradient boosting machines*, 2018 International Conference on Advances in Big Data, Computing and Data Communication Systems (icABCD), 2018.

(32) Wolff, B.; Kramer, O.; Heinemann, D. Selection of numerical weather forecast features for pv power predictions with random forests. *Lect. Notes Comput. Sci.* **2017**, *10097*, 78−91.

(33) Zhao, Z. M.; Li, C. H.; Shi, H.; Zou, Q. Material classification using random forest. *Adv. Mater. Res.* **2011**, *301−303*, 73−79.

(34) Quinlan, J. R. Induction of decision trees. *Mach. Learn.* **1986**, *1*, 81−106.

(35) Breiman, L. Bagging predictors. *Mach. Learn.* **1996**, *24*, 123−140.

(36) Plimpton, S. Fast parallel algorithms for short-range molecular-dynamics. *J. Comput. Phys.* **1995**, *117*, 1−19.

(37) Jiang, J.-W.; Zhou, Y.-P. *Parameterization of Stillinger-Weber potential for two- dimensional atomic crystals*; IntechOpen: London, 2017.

(38) Manzeli, S.; Ovchinnikov, D.; Pasquier, D.; Yazyev, O. V.; Kis, A. 2D transition metal dichalcogenides. *Nat. Rev. Mater.* **2017**, *2*, No. 17033.

(39) Gan, Y.; Zhao, H. Chirality and vacancy effect on phonon dispersion of MoS_2 with strain. *Phys. Lett. A* **2016**, *380*, 745−752.

(40) Zhou, Y.; Jiang, J. Molecular dynamics simulations for mechanical properties of borophene: parameterization of valence force field model and Stillinger-Weber potential. *Sci. Rep.* **2017**, *7*, No. 45516.

(41) Mortazavi, B. Ultra high stiffness and thermal conductivity of graphene like C_3N. *Carbon* **2017**, *118*, 25−34.

(42) Sha, Z.-D.; Pei, Q.-X.; Zhang, Y.-Y.; Zhang, Y.-W. Atomic vacancies significantly degrade the mechanical properties of phosphorene. *Nanotechnology* **2016**, *27*, No. 315704.

(43) Mortazavi, B.; Fan, Z.; Pereira, L. F. C.; Harju, A.; Rabczuk, T. Amorphized graphene: a stiff material with low thermal conductivity. *Carbon* **2016**, *103*, 318−326.

(44) Fang, T.; Chang, W.; Yang, J. Temperature effect on mechanical properties of graphene sheets under tensile loading. *Dig. J. Nanomater. Biostruct.* **2012**, *7*, 1811−1816.

(45) Zhurkov, S. N. Kinetic concept of the strength of solids. *Int. J. Fract.* **1984**, *26*, 295−307.

(46) Qiu, H.; Xu, T.; Wang, Z.; Ren, W.; Nan, H.; Ni, Z.; Chen, Q.; Yuan, S.; Miao, F.; Song, F.; Long, G.; Shi, Y.; Sun, L.; Wang, J.; Wang, X. Hopping transport through defect-induced localized states in molybdenum disulphide. *Nat. Commun.* **2013**, *4*, No. 2642.

(47) Hu, S.; Chen, J.; Yang, N.; Li, B. Thermal transport in graphene with defect and doping: phonon modes analysis. *Carbon* **2017**, *116*, 139−144.

(48) Rosenberger, M. R.; Chuang, H.-J.; McCreary, K. M.; Li, C. H.; Jonker, B. T. Electrical characterization of discrete defects and impact of defect density on photoluminescence in monolayer WS_2. *ACS Nano* **2018**, *12*, 1793−1800.

(49) Okada, M.; Sawazaki, T.; Watanabe, K.; Taniguch, T.; Hibino, H.; Shinohara, H.; Kitaura, R. Direct chemical vapor deposition growth of WS_2 atomic layers on hexagonal boron nitride. *ACS Nano* **2014**, *8*, 8273−8277.

(50) Gao, Y.; Liu, Z.; Sun, D.-M.; Huang, L.; Ma, L.-P.; Yin, L.-C.; Ma, T.; Zhang, Z.; Ma, X.-L.; Peng, L.-M.; Cheng, H.-M.; Ren, W. Large-area synthesis of high-quality and uniform monolayer WS_2 on reusable Au foils. *Nat. Commun.* **2015**, *6*, No. 8569.

(51) Zhou, W.; Zou, X.; Najmaei, S.; Liu, Z.; Shi, Y.; Kong, J.; Lou, J.; Ajayan, P. M.; Yakobson, B. I.; Idrobo, J.-C. Intrinsic structural defects in monolayer molybdenum disulfide. *Nano Lett.* **2013**, *13*, 2615−2622.

(52) Chu, K.; Wang, J.; Liu, Y. P.; Geng, Z. R. Graphene defect engineering for optimizing the interface and mechanical properties of graphene/copper composites. *Carbon* **2018**, *140*, 112−123.

(53) Kim, K.; Nam, K. H.; Lee, J.; Kim, H. J.; Goh, M.; Ku, B. C.; You, N. H. Effect of defect-healing in graphene nanosheets on the mechanical properties of polyimide nanocomposites. *Carbon* **2017**, *122*, 614−621.

(54) Gao, Y. F.; Jing, Y. H.; Liu, J. Q.; Li, X. C.; Meng, Q. Y. Tunable thermal transport properties of graphene by single-vacancy point defect. *Appl. Therm. Eng.* **2017**, *113*, 1419−1425.

(55) Tan, S. H.; Tang, L. M.; Xie, Z. X.; Pan, C. N.; Chen, K. Q. Effect of pentagon-heptagon defect on thermal transport properties in graphene nanoribbons. *Carbon* **2013**, *65*, 181−186.

(56) Ansari, R.; Ajori, S.; Motevalli, B. Mechanical properties of defective single-layered graphene sheets via molecular dynamics simulation. *Superlattices Microstruct.* **2012**, *51*, 274−289.

(57) Shirazi, A. H. N.; Abadi, R.; Izadifar, M.; Alajlan, N.; Rabczuk, T. Mechanical responses of pristine and defective C_3N nanosheets studied by molecular dynamics simulations. *Comput. Mater. Sci.* **2018**, *147*, 316−321.

(58) Dewapriya, M. A. N.; Rajapakse, R. K. N. D. Molecular dynamics simulations and continuum modeling of temperature and strain rate dependent fracture strength of graphene with vacancy defects. *J. Appl. Mech.* **2014**, *81*, No. 081010.